BMC Medical Imaging

RESEARCH

Open Access

Radiomics analysis of dual-layer detector spectral CT-derived iodine maps for predicting Ki-67 PI in pancreatic ductal adenocarcinoma

Dan Zeng[1†], Zuhua Song[1†], Qian Liu[1], Jie Huang[1], Xinwei Wang[1] and Zhuoyue Tang[1*]

Abstract

Objective To evaluate the feasibility of radiomics analysis using dual-layer detector spectral CT (DLCT)-derived iodine maps for the preoperative prediction of the Ki-67 proliferation index (PI) in pancreatic ductal adenocarcinoma (PDAC).

Materials and methods A total of 168 PDAC patients who underwent DLCT examination were included and randomly allocated to the training ($n=118$) and validation ($n=50$) sets. A clinical model was constructed using independent clinicoradiological features identified through multivariate logistic regression analysis in the training set. The radiomics signature was generated based on the coefficients of selected features from iodine maps in the arterial and portal venous phases of DLCT. Finally, a radiomics-clinical model was developed by integrating the radiomics signature and significant clinicoradiological features. The predictive performance of three models was evaluated using the Receiver Operating Characteristic (ROC) curve and Decision Curve Analysis. The optimal model was then used to develop a nomogram, with goodness-of-fit evaluated through the calibration curve.

Results The radiomics-clinical model integrating radiomics signature, CA19-9, and CT-reported regional lymph node status demonstrated excellent performance in predicting Ki-67 PI in PDAC, which showed an area under the ROC curve of 0.979 and 0.956 in the training and validation sets, respectively. The radiomics-clinical nomogram demonstrated the improved net benefit and exhibited satisfactory consistency.

Conclusions This exploratory study demonstrated the feasibility of using DLCT-derived iodine map-based radiomics to predict Ki-67 PI preoperatively in PDAC patients. While preliminary, our findings highlight the potential of functional imaging combined with radiomics for personalized treatment planning.

Keywords Dual-layer detector spectral computed tomography, Iodine map, Ki-67, Pancreatic ductal adenocarcinoma, Radiomics

[†]Dan Zeng and Zuhua Song contributed equally as co-first author to this work.

*Correspondence:
Zhuoyue Tang
zhuoyue_tang@cqu.edu.cn
[1]Department of Radiology, Chongqing General Hospital, Chongqing, China

Introduction

Pancreatic ductal adenocarcinoma (PDAC) is a highly malignant disease with a 5-year survival rate of <12%. It is projected to become the second-leading cause of cancer-related deaths by 2030 [1, 2]. Ki-67 is a marker to distinguish between proliferating and non-proliferating cells [3]. A high Ki-67 proliferation index (PI) has been shown to correlate with reduced overall survival and recurrence-free survival [4, 5]. Preoperatively identifying PDAC patients with high Ki-67 PI and implementing neoadjuvant therapy may result in better clinical benefits than performing upfront surgery.

While immunohistochemical (IHC) examination is a standard method for assessing Ki-67 PI in PDAC, limitations such as small sample sizes in biopsies, tumor heterogeneity, and the operator's technical proficiency and experience can affect the results [6, 7]. In addition, the invasive nature of obtaining biopsy and surgical specimens exacerbates these challenges, whereas non-invasive imaging techniques such as CT offer a promising alternative. If CT imaging modalities demonstrate an association between Ki-67 PI and PDAC characteristics, they could serve as indirect prognostic indicators. This could help identify PDAC patients who may benefit from more aggressive therapeutic interventions.

Radiomics, which enables the extraction of high-dimensional quantitative features from standard medical images, has shown great promise in tumor characterization, risk stratification, and prognosis prediction across various malignancies [8, 9]. However, most radiomics studies in PDAC rely on conventional CT or MRI, with limited functional information. The emergence of dual-layer spectral detector CT (DLCT) allows for material decomposition and the generation of iodine maps, providing functional insights into tumor perfusion and vascularity. DLCT-derived quantitative parameters have demonstrated utility in predicting tumor stage, lymph node (LN) metastasis, and histological differentiation in PDAC [10–12], while DLCT-based radiomics has shown potential in evaluating tumor heterogeneity and metastatic potential [10, 13].

Despite these advancements, few studies have investigated the potential of DLCT-based radiomics for predicting Ki-67 PI in PDAC. Our group has previously demonstrated the feasibility of using both conventional CT radiomics and DLCT-derived parameters for this purpose [14–16]. Building on these efforts, we hypothesize that variations in Ki-67 PI reflect microscopic changes in tumor perfusion heterogeneity, which can be quantitatively captured by radiomics features extracted from DLCT-derived iodine maps. The arterial phase (AP) and portal venous phase (PVP) provide complementary information on tumor vascularity, and their combined analysis may enhance the assessment of perfusion patterns and tumor aggressiveness. Previous studies have confirmed that dual-phase radiomics improves prognostic prediction in PDAC [17–19]. Therefore, this study aims to investigate whether radiomics features derived from dual-phase DLCT iodine maps can serve as non-invasive biomarkers for preoperatively predicting Ki-67 PI in PDAC patients.

Materials and methods

Patients

The study was approved by the institutional review board of Chongqing General Hospital, with a waiver of written informed consent due to the retrospective study design. Between July 2021 and December 2023, patients diagnosed with pathologically confirmed PDAC were enrolled. As depicted in Fig. 1, patients were eligible for the study if they (a) had a histopathologically confirmed diagnosis of PDAC; (b) obtained Ki-67 PI through IHC; and (c) underwent DLCT scans within 2 weeks at our institution before the IHC. Patients were ineligible if they (a) had received any relevant treatment (radiotherapy, chemotherapy, or chemoradiotherapy) before IHC; (b) had nondiagnostic CT image quality; (c) had coexisting other primary malignancies; or (d) had partially missing DLCT images or clinicopathological data.

Immunohistochemical analysis of Ki-67 PI

Standard IHC examination was performed on specimens obtained from fine needle aspiration or surgery to detect Ki-67 PI in all 168 patients. Positive cells were identified as those with a brown nucleus. Ki-67 PI was assessed by calculating the percentage of positive cells among 1,000 malignant cells at 200 × magnification. In the absence of a predetermined optimal threshold, we adopted a threshold of 50%, as suggested by previous research [20]. In our study, PDAC was categorized into either the low Ki-67 PI group (<50%) or the high Ki-67 PI group (≥50%).

DLCT image acquisition

All patients underwent DLCT examinations at our institution, with detailed scan protocols provided in the Supplementary Materials.

Evaluation of clinical features and CT imaging signs

Clinical features, including gender, age, body mass index, carbohydrate antigen (CA) 19–9, CA125, and carcinoembryonic antigen (CEA), were retrieved for each patient from the hospital information system.

All CT imaging signs were independently analyzed by two abdominal radiologists (hereinafter referred to as Radiologists A and B), with 7 and 11 years of experience, respectively. They remained blinded to clinical and pathological details throughout the evaluation process. The final results were determined by consensus between

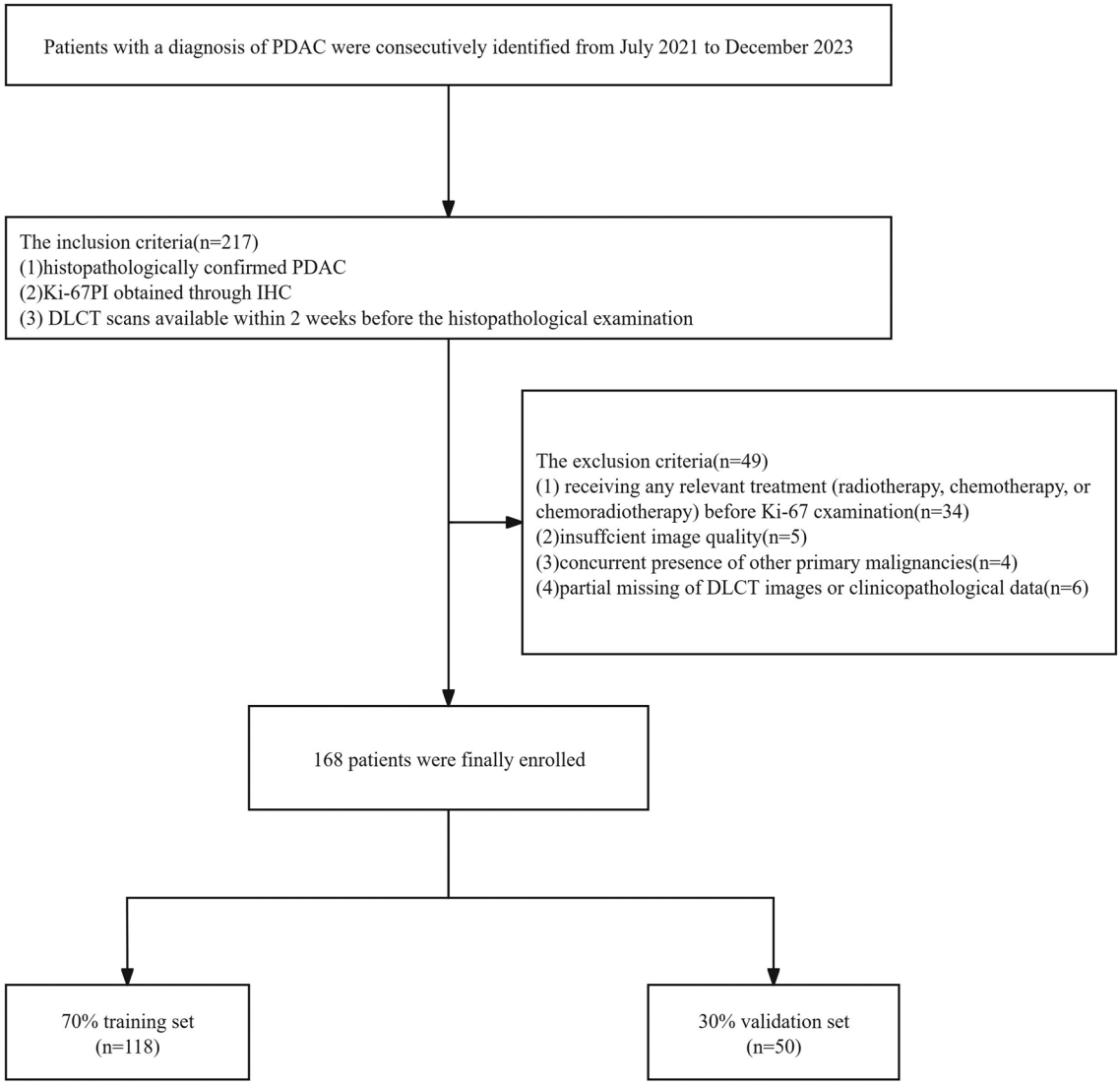

Fig. 1 Flowchart of the study population. PDAC, pancreatic ductal adenocarcinoma; IHC, immunohistochemistry; DLCT, dual-layer detector spectral computed tomography; PI, proliferation index

the two radiologists. The candidate CT imaging signs of PDAC included CT-reported T stage, CT-reported regional LN status, vascular invasion, and extrapancreatic perineural invasion. The evaluation criteria for each imaging sign are described in the Supplementary Materials.

Volumes of interest (VOI) segmentation

The workflow for establishing the key steps of the radiomics signature is illustrated in Fig. 2. Radiologist A used 3D Slicer (open-source software, version 5.6.2, https://www.slicer.org/) to manually delineate tumor contours slice by slice on PVP images, then transferred the contours from PVP images to AP images. If there were contour mismatches due to respiratory motion, manual adjustments were made to align the replicas with the contours observed in the PVP. Two weeks later, 30 cases were randomly selected, and segmentation was repeated by two radiologists (A and B) to assess intra- and interobserver reproducibility. Neither radiologist was aware of the histopathological results. Features with inter- and intraobserver correlation coefficients (ICCs) greater than 0.75 were considered sufficiently consistent for further analysis.

Radiomics extraction and selection

All radiomics analyses were implemented with FeAture Explorer Pro (FAE, V 0.5.14) on Python (3.7.6) [21]. Both AP and PVP DLCT-derived iodine maps were used for radiomics feature extraction. Before feature extraction, the CT images were resampled to a standardized pixel dimension of $1.0 \times 1.0 \times 1.0$ mm^3 and normalized to a

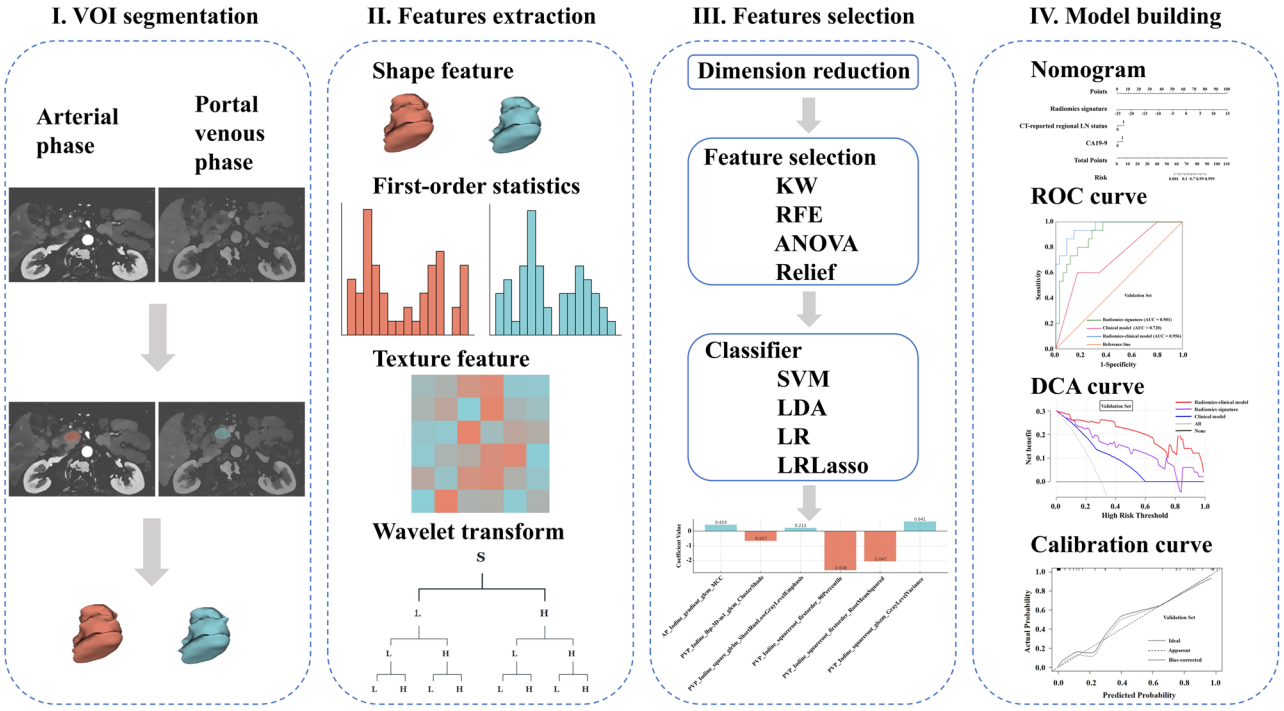

Fig. 2 Workflow of the key steps in conducting radiomics analysis of iodine maps. DCA, decision curve analysis; KW, Kruskal-Wallis; RFE, recursive feature elimination; ANOVA, analysis of variance; SVM, support vector machines; LDA, linear discriminant analysis; LR, logistic regression; LRLasso, lasso logistic regression; ROC, receiver operating characteristic; VOI, volumes of interest; LN, lymph node; CA19-9, carbohydrate antigen 19–9; AUC, area under the curve

scale of 1000. Gray-level discretization was applied to the original intensities by resampling them into 25 fixed bins. The processed images were subjected to various transformations using wavelet, square root, square, logarithm, gradient, exponential, Laplacian of Gaussian, and local binary pattern (3D) filters. The extracted features in this study included shape-based features, first-order statistical features (e.g., maximum, skewness, mean, median), and multiple texture matrices, including the gray-level co-occurrence matrix (GLCM), gray-level dependence matrix (GLDM), gray-level run length matrix (GLRLM), gray-level size zone matrix (GLSZM), and neighboring gray tone difference matrix (NGTDM).

First, Z-score normalization was applied to features with ICCs greater than 0.75. Second, the Pearson correlation coefficient (PCC) was used to measure the correlation between each pair of features and to reduce dimensionality. If the PCC exceeded 0.99, one of the redundant features was randomly removed. Finally, feature selection was conducted using techniques including Kruskal-Wallis, Relief, recursive feature elimination (RFE), and analysis of variance (ANOVA). All these methods (KW, Relief, RFE, ANOVA) were applied for feature selection. We constructed multiple model pipelines, where each pipeline consisted of: (1) a feature selection method (KW, Relief, RFE, ANOVA), (2) a machine learning model (support vector machines (SVM), linear discriminant analysis (LDA), logistic regression (LR), and lasso logistic regression (LRLasso)) (Table S1), and (3) varying numbers of features (from 1 to 15). The performance of each pipeline was evaluated using 10-fold cross-validation. The discrimination performance was evaluated using the receiver operating characteristic (ROC) curve, and the radiomics signature that demonstrated the best predictive performance in the validation set was chosen as the optimal signature (The detailed parameter configuration of ML algorithms can be found in the Supplementary Materials).

Development of the clinical model and radiomics-clinical nomogram

First, the clinicoradiological features (i.e., the clinical features and CT imaging signs) between the high and low Ki-67 PI groups were compared using the Chi-square test, Mann-Whitney U test, and two-sample t test. Then, significant factors with $p < 0.05$ from univariate analysis were included in multivariate logistic regression (LR) analysis to determine the independent factors for constructing the clinical model in the training set.

The radiomics-clinical nomogram was developed by integrating the radiomics signature from dual-phase iodine maps and significant clinicoradiological features using multivariate LR. The odds ratio (OR) and 95% confidence interval (CI) were calculated for each independent predictive factor.

Assessment of the performance of the different models

The area under the curve (AUC) with 95% CI, sensitivity, and specificity was used to assess the performance of the three models (clinical model, radiomics signature, and radiomics-clinical nomogram) in both the training and validation sets. The DeLong test was applied to compare the AUCs of the three models. Subsequently, a nomogram was constructed using the optimal model. Decision curve analysis (DCA) was conducted to evaluate the clinical usefulness of the three models by quantifying their net benefits across different threshold probabilities in the validation set. Finally, the calibration curve and Hosmer-Lemeshow test were used to evaluate the calibration performance of the nomogram in both the training and validation sets.

Statistical analysis

All statistical analyses and calculations were performed using R software (http://www.R-project.org), SPSS (version 26.0, IBM), and MedCalc (version 18.2.1, MedCalc Software). The Shapiro-Wilk test was used to assess data normality. Normally distributed data were presented as mean ± standard deviation (SD), while non-normally distributed data were expressed as median (25th, 75th percentiles). Categorical variables were analyzed using the Chi-square test, and continuous variables were assessed using either the Mann-Whitney U test or the two-sample t test. Statistical significance was defined as a two-sided p-value < 0.05.

Table 1 Clinicoradiological features of PDAC patients

Features	Training set (n = 118)	Validation set (n = 50)	*p*
Age, y	61.5(55,70)	63.5(53,68.25)	0.647
BMI	22.15(20.28,24.31)	21.87(20.80,24.72)	0.690
Gender, *n* (%)			0.926
Male	67(56.8)	28(56.0)	
Female	51(43.2)	22(44.0)	
CA19-9, *n* (%)			0.088
Normal	47(39.8)	13(26.0)	
Elevated	71(60.2)	37(74.0)	
CEA, *n* (%)			0.104
Normal	90(76.3)	32(64.0)	
Elevated	28(23.7)	18(36.0)	
CA125, *n* (%)			0.539
Normal	79(66.9)	31(62.0)	
Elevated	39(33.1)	19(38.0)	
CT-reported T stage			0.613
T1-2	45(38.1)	17(34.0)	
T3-4	73(61.9)	33(66.0)	
CT-reported regional LN status			0.729
Negative	65(55.1)	29(58.0)	
Positive	53(44.9)	21(42.0)	
vascular invasion			0.286
Negative	53(44.9)	18(36.0)	
Positive	65(55.1)	32(64.0)	
extrapancreatic perineural invasion			0172
Negative	41(34.7)	12(24.0)	
Positive	77(65.3)	38(76.0)	

CT, computed tomography; PDAC, pancreatic ductal adenocarcinoma; BMI, body mass index; CA125, carbohydrate antigen 125; CA19-9, carbohydrate antigen 19–9; CEA, carcinoembryonic antigen; LN lymph node

Results

Patient characteristics

A total of 168 patients were analyzed, with 118 in the training set and 50 in the validation set. The rates of low and high Ki-67 were 70.3% (83/118) and 29.7% (35/118) in the training set and 70.0% (35/50) and 30.0% (15/50) in the validation set, respectively. There were no significant differences between the training and validation sets in any clinicoradiological features (Table 1; all $p > 0.05$).

Clinical model development

Table 2 presents the results of the univariate and multivariate LR analyses between the high and low Ki-67 PI groups in the training set. The univariate analysis showed significant associations of CA19-9, CT-reported regional LN status, and extrapancreatic perineural invasion with Ki-67 PI ($p < 0.05$). Furthermore, stepwise multivariate LR analysis identified CA19-9 and CT-reported regional LN status as independent predictors of Ki-67 PI (Table 3). Consequently, a clinical model was developed based on these two predictors.

Feature selection and radiomics signature building

Among the 2,622 dual-phase radiomics features, 1,982 stable features (974 from AP and 1,008 from PVP) with an ICC greater than 0.75 were retained for further analysis (Fig. S1). In constructing the radiomics signature, a pipeline utilizing Z-score normalization, PCC dimension reduction, RFE feature selection, and LR classifier identified six features: two first-order statistical features and four textural features. These features were included in the radiomics signature, which demonstrated optimal predictive performance. The composition and contribution of these features are illustrated in Fig. 3.

Following the multivariate LR analysis, we found that the radiomics signature (OR = 2.975; 95% CI: 1.724–5.134; $p < 0.001$), CA19-9 (OR = 7.734; 95% CI: 1.053–56.793; $p = 0.044$), and CT-reported regional LN status (OR = 11.461; 95% CI: 1.992–65.948; $p = 0.006$) were independent predictors for Ki-67 PI ($p < 0.05$) in the training set (Table 3). All these predictors were incorporated into the radiomics-clinical model and visualized as a nomogram, as shown in Fig. 4.

Table 2 Univariate analysis to differentiate between high and low Ki-67 PI groups in the training set

Variables	High Ki-67 PI group (Ki-67 PI ≥ 50%, n = 35)	Low Ki-67 PI group (Ki-67 PI < 50%, n = 83)	F/Z/c²	*p*
Age, y	65(58,70)	22.49(21.33,24.31)	−1.182	0.237
BMI	22.49(21.33,24.31)	21.87(20.80,24.72)	−0.884	0.377
Gender, *n* (%)			3.619	0.391
Male	67(56.8)	28(56.0)		
Female	51(43.2)	22(44.0)		
CA19-9, *n* (%)			84.828	<0.001
Normal	47(39.8)	13(26.0)		
Elevated	71(60.2)	37(74.0)		
CEA, *n* (%)			5.503	0.205
Normal	90(76.3)	32(64.0)		
Elevated	28(23.7)	18(36.0)		
CA125, *n* (%)			1.268	0.543
Normal	79(66.9)	31(62.0)		
Elevated	39(33.1)	19(38.0)		
CT-reported T stage			2.795	0.275
T1-2	45(38.1)	17(34.0)		
T3-4	73(61.9)	33(66.0)		
CT-reported regional LN status				
Negative	65(55.1)	29(58.0)	3.990	<0.001
Positive	53(44.9)	21(42.0)		
vascular invasion			12.993	0.056
Negative	53(44.9)	18(36.0)		
Positive	65(55.1)	32(64.0)		
extrapancreatic perineural invasion			28.635	0.029
Negative	41(34.7)	12(24.0)		
Positive	77(65.3)	38(76.0)		
Radiomics signature	3.75 ± 2.79	−3.67 ± 4.66	3.656	<0.001

BMI, body mass index; PI, proliferation index; CA125, carbohydrate antigen 125; CA19-9, carbohydrate antigen 19–9; CEA, carcinoembryonic antigen; LN lymph node

Table 3 Multivariate logistic regression analysis in the training set

Variables	Odds ratio	95%CI	*p*
Radiomics signature	2.975	1.724–5.134	<0.001
CT-reported regional LN status	11.461	1.992–65.948	0.006
CA19-9	7.734	1.053–56.793	0.044

CI, confidence interval; CA19-9, carbohydrate antigen 19–9; LN lymph node

Comparison of the predictive performance among models

The predictive performance of the three models is summarized in Table 4, including AUC, sensitivity, specificity, and DeLong test results. ROC analyses conducted to distinguish high and low Ki-67 PI in both the training and validation sets for the three models are shown in Fig. 5. The clinical model exhibited good diagnostic effectiveness in predicting Ki-67 PI among PDAC patients, achieving an AUC of 0.805 (95% CI: 0.724–0.886) in the training set, while demonstrating moderate effectiveness with an AUC of 0.720 (95% CI: 0.574–0.866) in the validation set. Both the radiomics signature and the radiomics-clinical model demonstrated excellent diagnostic effectiveness in predicting Ki-67 PI in PDAC, with AUCs of 0.957 (95% CI: 0.926–0.988) and 0.979 (95% CI: 0.961–0.998) in the training set, respectively. In the validation set, the radiomics signature and the radiomics-clinical model achieved AUCs of 0.901 (95% CI: 0.817–0.985) and 0.956 (95% CI: 0.904–1.000), respectively. The DeLong test indicated a significant improvement in the AUC of the radiomics-clinical model compared to the clinical model in both the training set ($p < 0.001$) and the validation set ($p = 0.002$). Additionally, a significant difference was observed between the radiomics signature and the clinical model in the training set ($p < 0.001$), but this difference was not statistically significant in the validation set ($p = 0.057$). In terms of clinical benefit, DCA demonstrated that the radiomics-clinical model provided a greater net benefit across a threshold probability range of 0.05–0.95, compared to both the clinical model and radiomics signature, indicating superior clinical utility (Fig. 6). The calibration curves for the radiomics-clinical model demonstrated strong alignment between predicted and observed outcomes in both sets (Fig. 7). The Hosmer-Lemeshow test showed no significant difference ($p = 0.952$ for the training set and $p = 0.728$ for the validation set), indicating that the nomogram was well-calibrated without significant deviation from the ideal fit.

Discussion

In this retrospective study, we built upon our team's prior investigations to develop a radiomics signature based on dual-phase DLCT-derived iodine maps for predicting Ki-67 PI in PDAC patients. Furthermore, the radiomics-clinical model, integrating radiomics signature and independent clinicoradiological features, demonstrated superior predictive performance compared to either the radiomics signature or clinical model alone. This combined approach offers an effective and non-invasive method for the preoperative prediction of Ki-67 PI in PDAC patients.

The present study builds upon our previous work investigating imaging-based prediction of Ki-67 PI in PDAC. Li et al. demonstrated the feasibility of conventional CT radiomics, while subsequent studies explored the predictive value of DLCT-derived quantitative parameters [14–16]. Extending these efforts, the current research integrates dual-phase (arterial and portal venous) iodine

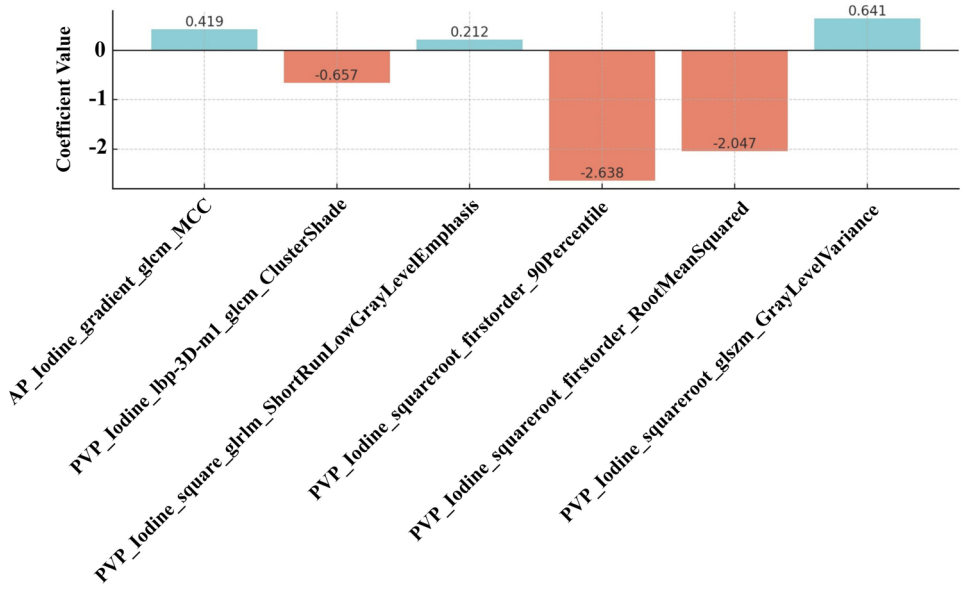

Fig. 3 Radiomics feature selection results. AP, arterial phase; PVP, portal venous phase; GLCM, gray-level co-occurrence matrix; GLRLM, gray-level run length matrix; GLSZM, gray-level size zone matrix

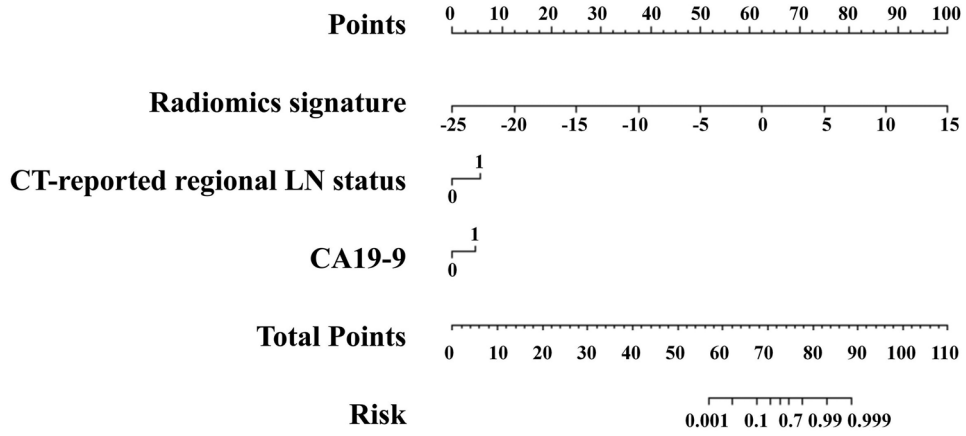

Fig. 4 Radiomics-clinical nomogram developed in the training set, incorporating the radiomics signature, CA19-9, and CT-reported regional LN status. CA19-9, carbohydrate antigen 19–9; LN, lymph node

Table 4 Predictive performance of the clinical model, radiomics signature, and radiomics-clinical models

Models	Training set				Validation set			
	AUC (95%CI)	SEN	SPE	DeLong	AUC (95%CI)	SEN	SPE	DeLong
Clinical model	0.805 (0.724–0.886)	0.657	0.855	<0.001#	0.720 (0.574–0.866)	0.600	0.829	0.057#
Radiomics signature	0.957 (0.926–0.988)	0.971	0.771	0.032##	0.901 (0.817–0.985)	0.800	0.800	0.038##
Radiomics-clinical model	0.979 (0.961–0.998)	0.971	0.880	< 0.001###	0.956 (0.904–1.000)	0.933	0.857	0.002###

AUC, area under the receiver operating characteristic curve; CI, confidence interval; SEN, sensitivity; SPE specificity

#Clinical model versus Radiomics signature

##Radiomics signature versus Radiomics-clinical model

###Radiomics-clinical model versus Clinical model

maps derived from DLCT with advanced radiomics analysis to more comprehensively characterize tumor heterogeneity. Compared with conventional CT, DLCT iodine maps provide functional insights by separating iodine content from tissue attenuation, enabling a more accurate evaluation of tumor vascularity and perfusion [14, 22]. Dual-phase imaging captures complementary perfusion features—arterial phase reflects early vascularization, while portal venous phase offers additional information on tissue perfusion—thereby enhancing the assessment

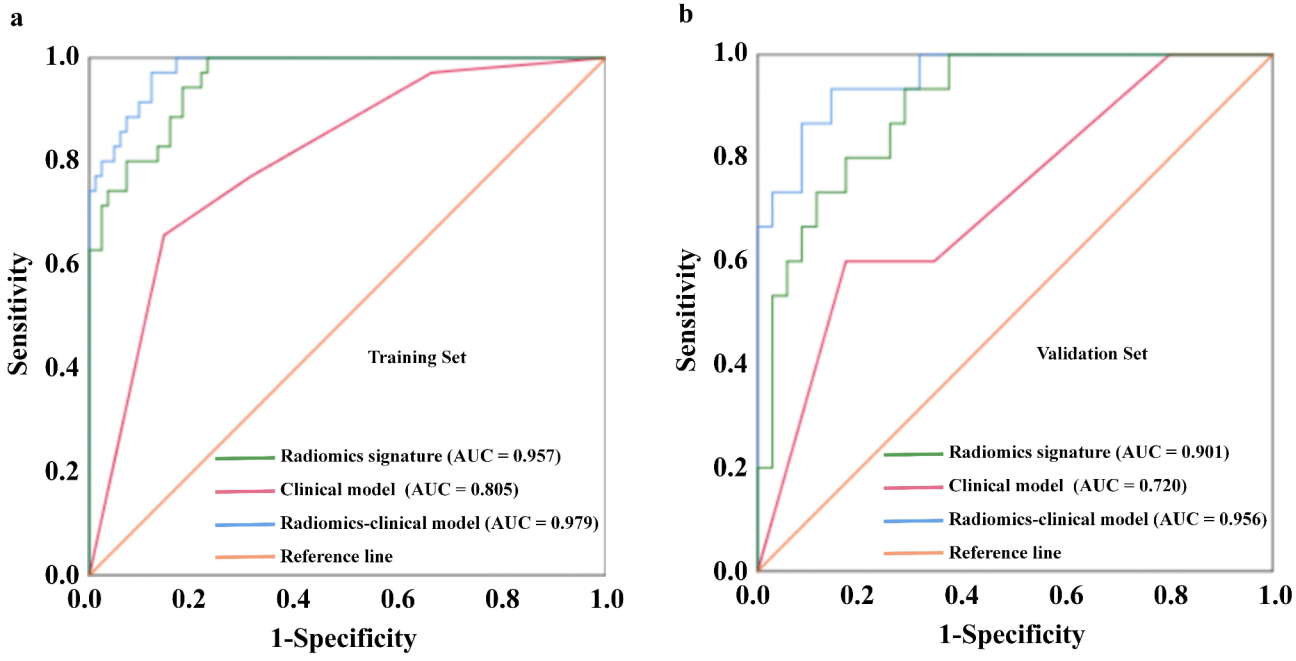

Fig. 5 ROC curves depicting the predictive performance of the clinical model, radiomics signature, and radiomics-clinical models for Ki-67 PI in PDAC (**a, b**). AUC, area under the curve; PI, proliferation index; PDAC, pancreatic ductal adenocarcinoma; ROC, receiver operating characteristic

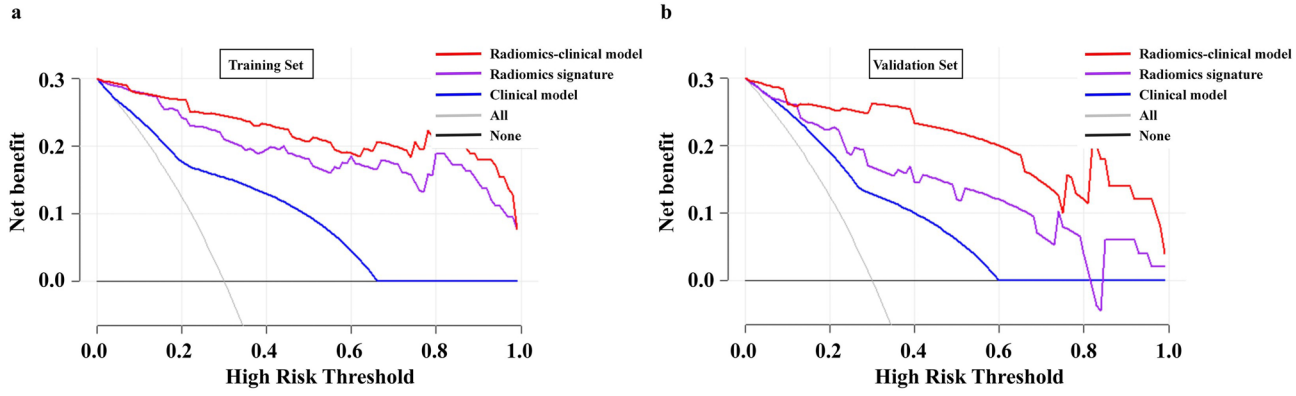

Fig. 6 DCA results for the clinical model, radiomics signature, and radiomics-clinical models (**a, b**). DCA, decision curve analysis

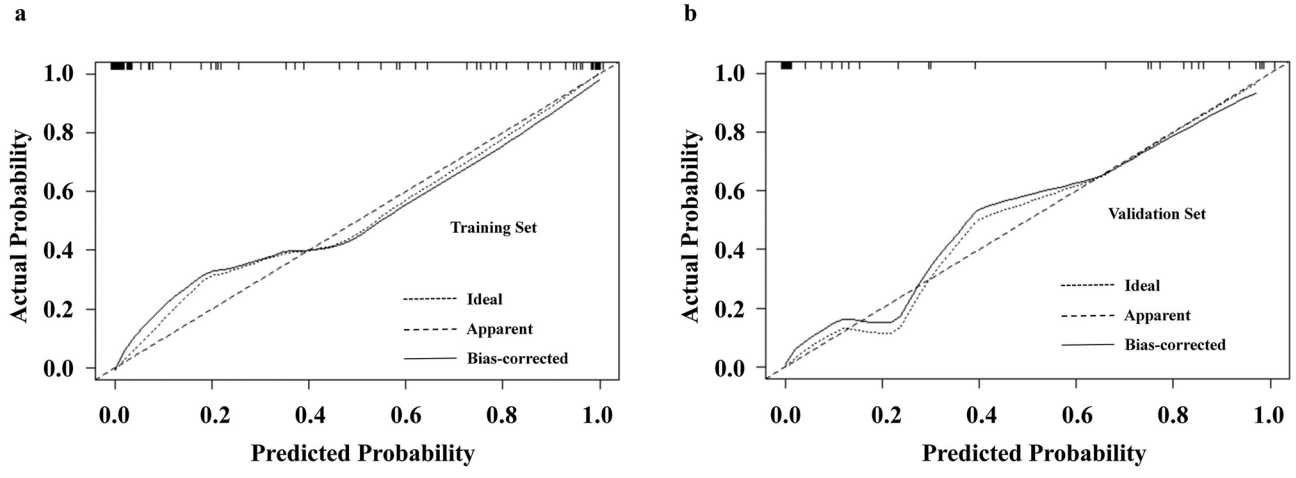

Fig. 7 Calibration curves of the radiomics-clinical nomogram (**a, b**)

of tumor aggressiveness. Furthermore, unlike previous DLCT-based studies that did not incorporate clinical variables, our model integrates key clinicoradiological features such as CA19-9 and CT-reported regional LN status [15, 16], thereby improving the predictive performance and clinical applicability of the model.

Building on our prior findings, we further validated CA19-9 and CT-reported regional LN status as independent predictors of Ki-67 PI through multivariate analysis [14]. CA19-9 is a recognized prognostic marker in PDAC, with elevated levels linked to poor differentiation and outcomes [23, 24]. Ki-67 PI reflects tumor proliferative activity, with higher values indicating greater aggressiveness and worse prognosis [5, 25]. In this study, the high Ki-67 PI group showed significantly higher CA19-9 levels and CT-reported regional LN positivity (72.0% vs. 32.2%), consistent with reports associating high Ki-67 expression with increased regional LN metastasis [26, 27]. The strong correlation between CT-reported and pathological LN status further supports the reliability of imaging for LN assessment [4, 13, 28]. This association likely reflects the role of Ki-67 in tumor proliferation and lymphatic invasion, indicating that CT-reported regional LN status may serve as a non-invasive surrogate for Ki-67 PI. The clinical model incorporating CA19-9 and LN status achieved good performance in the training set (AUC = 0.805), but only moderate performance in the validation set (AUC = 0.720), suggesting that combining tumor markers and morphological features alone may be insufficient, and that integrating perfusion or intratumoral characteristics could improve predictive performance.

DLCT enhances CT diagnostics by enabling functional imaging through iodine maps, which accurately depict lesion vascularity and improve contrast between hypoattenuating tumors and normal parenchyma [29]. Radiomics extracts high-throughput quantitative features that reflect intratumoral perfusion heterogeneity, leveraging DLCT's functional information [30, 31]. Prior studies have applied DLCT-based radiomics to predict LN metastasis, tumor stage, and differentiation in PDAC [10–13], highlighting its clinical potential. Unlike these studies, our work focuses on Ki-67 PI, a key marker of tumor proliferation. We developed a radiomics signature based on dual-phase iodine maps, achieving excellent performance in both training (AUC = 0.957) and validation sets (AUC = 0.901). Among six selected features, five were from the PVP and one from the AP, aligning with findings that PVP images better capture PDAC biology and enhance tumor delineation [32–34]. Texture features predominated, consistent with prior studies [14], likely due to their ability to quantify spatial heterogeneity. Specifically, GLCM captures local texture variation, GLRLM reflects fine texture continuity, and GLSZM characterizes larger structural patterns [35–37]. These features provide a comprehensive view of tumor heterogeneity relevant to proliferation and prognosis. Notably, first-order features, while fewer, showed higher importance, offering direct intensity-based information with strong reproducibility across imaging conditions [38–40]. The integration of texture and first-order features balances biological insight and robustness, supporting clinical applicability.

To enhance predictive performance, the radiomics signature was combined with CA19-9 and CT-reported regional LN status to construct a radiomics-clinical model, which achieved the highest AUCs in both training (0.979) and validation (0.956) sets, outperforming the radiomics and clinical models alone. The improvement over the clinical model was statistically significant ($p < 0.001$ and $p = 0.002$, respectively). This enhancement likely stems from the model's ability to capture tumor aggressiveness and heterogeneity via iodine map-derived features. DCA demonstrated superior net benefit of the radiomics-clinical model, supporting its clinical utility. Calibration curves showed good agreement between predicted and observed probabilities, with a nonsignificant Hosmer-Lemeshow test ($p = 0.384$), indicating satisfactory model fit. These results suggest that integrating radiomics and clinical features offers complementary value and significantly improves the prediction of Ki-67 PI in PDAC.

Despite promising results, this single-center study should be considered preliminary. As one of the few studies focusing on preoperative Ki-67 prediction in PDAC, it provides a foundation for future multicenter validation. Expanding to multiple institutions and assessing radiomics feature stability across different scanners, acquisition protocols, and reconstruction settings will be key to confirming model reproducibility and generalizability. Additionally, we are actively working to expand collaborations with other hospitals to promote Ki-67 IHC testing and DLCT scanning, which are essential for validating our approach. These efforts will facilitate the broader application of our model and support its prospective validation in independent cohorts, ensuring its clinical reliability and practical utility. Thirdly, future work may explore automated segmentation using deep learning combined with expert refinement to enhance reproducibility while maintaining clinical interpretability.

Conclusion

In conclusion, the radiomics-clinical model which integrates the radiomics signature from DLCT-derived iodine maps with clinicoradiological features exhibited excellent performance in preoperatively predicting Ki-67 PI in PDAC patients. This may help clinicians identify PDAC patients with high Ki-67 PI and facilitate personalized treatment strategies. However, it is important

to note that these findings are preliminary and require external validation through multi-center studies to confirm their applicability and robustness in clinical practice.

Abbreviations

AP	Arterial phase
AUC	Area under the curve
CA125	Carbohydrate antigen 125
CA19-9	Carbohydrate antigen 19-9
CEA	Carcinoembryonic antigen
CI	Confidence interval
DCA	Decision curve analysis
DLCT	Dual-layer detector spectral CT
ICC	Intraclass correlation coefficient
IHC	Immunohistochemical
LN	Lymph node
LR	Logistic regression
OR	Odds ratio
PCC	Pearson correlation coefficient
PDAC	Pancreatic ductal adenocarcinoma
PI	Proliferation index
PVP	Portal venous phase
RFE	Recursive feature elimination
ROC	Receiver operating characteristic
VMI	Virtual monoenergetic image
VOI	Volumes of interest

Supplementary Information

The online version contains supplementary material available at https://doi.org/10.1186/s12880-025-01664-7.

Supplementary Material 1

Acknowledgments
Not applicable.

Author contributions
D Z, ZH S, and ZY T proposed the design of the study. Q L, J H, and XW W collected the data. D Z and ZH S analyzed the data. D Z wrote the first draft. All authors read and approved the final manuscript.

Data Availability
The datasets generated and/or analyzed during the current study are not publicly available due to the hospital policy but are available from the corresponding author on reasonable request.

Declarations

Ethics approval and consent to participate
The research adhered to the Declaration of Helsinki and its latest amendments. Approval was granted by the Ethics Committee of Chongqing General Hospital (approval number KY S2023-070-01), and the need for informed consent was waived owing to the retrospective study design.

Funding
This study was supported by the Medical Research Program of the combination of Chongqing National Health Commission and Chongqing Science and Technology Bureau, China (2024QNXM058) and the Key Special Program of Technological Innovation and Application Development in Chongqing, China (no. CSTB2023TIAD-KPX0059-2).

Consent for publication
Not applicable.

Competing interests
The authors declare no competing interests.

Received: 24 October 2024 / Accepted: 7 April 2025
Published online: 17 April 2025

References

1. Rahib L, Smith BD, Aizenberg R, Rosenzweig AB, Fleshman JM, Matrisian LM. Projecting cancer incidence and deaths to 2030: the unexpected burden of thyroid, liver, and pancreas cancers in the United States. Cancer Res. 2014;74:2913–21.
2. Siegel RL, Miller KD, Wagle NS, Jemal A. Cancer statistics, 2023. CA Cancer J Clin. 2023;73:17–48.
3. Scholzen T, Gerdes J. The Ki-67 protein: from the known and the unknown. J Cell Physiol. 2000;182:311–22.
4. Jamieson NB, Carter CR, McKay CJ, Oien KA. Tissue biomarkers for prognosis in pancreatic ductal adenocarcinoma: a systematic review and meta-analysis. Clin Cancer Res. 2011;17:3316–31.
5. Liang Y, Sheng G, Guo Y, Zou Y, Guo H, Li Z, et al. Prognostic significance of grade of malignancy based on histopathological differentiation and Ki-67 in pancreatic ductal adenocarcinoma. Cancer Biol Med. 2024;21:416–32.
6. Wood LD, Canto MI, Jaffee EM, Simeone DM. Pancreatic cancer: pathogenesis, screening, diagnosis, and treatment. Gastroenterology. 2022;163:386–402.e1.
7. Trindade AJ, Benias PC, Alshelleh M, Bazarbashi AN, Tharian B, Inamdar S, et al. Fine-needle biopsy is superior to fine-needle aspiration of suspected gastrointestinal stromal tumors: a large multicenter study. Endosc Int Open. 2019;7:E931–6.
8. Mayerhoefer ME, Materka A, Langs G, Häggström I, Szczypiński P, Gibbs P, et al. Introduction to radiomics. J Nucl Med. 2020;61:488–95.
9. Limkin EJ, Sun R, Dercle L, Zacharaki EI, Robert C, Reuzé S, et al. Promises and challenges for the implementation of computational medical imaging (radiomics) in oncology. Ann Oncol. 2017;28:1191–206.
10. Wu L, Cen C, Yue X, Chen L, Wu H, Yang M, et al. A clinical-radiomics nomogram based on dual-layer spectral detector CT to predict cancer stage in pancreatic ductal adenocarcinoma. Cancer Imaging. 2024;24:55.
11. Chen Y, Xie T, Chen L, Zhang Z, Wang Y, Zhou Z, et al. The preoperative prediction of lymph node metastasis of resectable pancreatic ductal adenocarcinoma using dual-layer spectral computed tomography. Eur Radiol. 2024. https://doi.org/10.1007/s00330-024-11143-2.
12. Liu W, Xie T, Chen L, Tang W, Zhang Z, Wang Y, et al. Dual-layer spectral detector CT: a noninvasive preoperative tool for predicting histopathological differentiation in pancreatic ductal adenocarcinoma. Eur J Radiol. 2024;173:111327.
13. An C, Li D, Li S, Li W, Tong T, Liu L, et al. Deep learning radiomics of dual-energy computed tomography for predicting lymph node metastases of pancreatic ductal adenocarcinoma. Eur J Nucl Med Mol Imaging. 2022;49:1187–99.
14. Li Q, Song Z, Li X, Zhang D, Yu J, Li Z, et al. Development of a CT radiomics nomogram for preoperative prediction of Ki-67 index in pancreatic ductal adenocarcinoma: a two-center retrospective study. Eur Radiol. 2023. https://doi.org/10.1007/s00330-023-10393-w.
15. Wen Y, Song Z, Li Q, Zhang D, Li X, Yu J, et al. Development and validation of a model for predicting the expression of Ki-67 in pancreatic ductal adenocarcinoma with radiological features and dual-energy computed tomography quantitative parameters. Insights Imaging. 2024;15:41.
16. Zeng D, Zhang J, Song Z, Li Q, Zhang D, Li X, et al. Development and validation of a model based on preoperative dual-layer detector spectral computed tomography 3D VOI-based quantitative parameters to predict high Ki-67 proliferation index in pancreatic ductal adenocarcinoma. Insights Imaging. 2024;15:291.
17. De Robertis R, Geraci L, Tomaiuolo L, Bortoli L, Beleù A, Malleo G, et al. Liver metastases in pancreatic ductal adenocarcinoma: a predictive model based on CT texture analysis. Radiol Med. 2022;127:1079–84.
18. Cen C, Liu L, Li X, Wu A, Liu H, Wang X, et al. Pancreatic ductal adenocarcinoma at CT: a combined nomogram model to preoperatively predict cancer stage and survival outcome. Front Oncol. 2021;11:594510.
19. H Y, Z H, C L, D Q, C D, L G, et al. Contrast-enhanced CT radiomics combined with multiple machine learning algorithms for preoperative identification of lymph node metastasis in pancreatic ductal adenocarcinoma. Front Oncol. 2024;14:1342317.
20. Zhu X, Cao Y, Ju X, et al. Personalized designs of adjuvant radiotherapy for pancreatic cancer based on molecular profiles. Cancer Sci 2021;112:287–95.

21. Song Y, Zhang J, Zhang Y-D, Hou Y, Yan X, Wang Y, et al. FeAture explorer (FAE): a tool for developing and comparing radiomics models. PLoS One. 2020;15:e0237587.
22. McCollough CH, Leng S, Yu L, Fletcher JGD, Multi-Energy CT. Principles, technical approaches, and clinical applications. Radiology. 2015;276:637–53.
23. Chan A, Prassas I, Dimitromanolakis A, Brand RE, Serra S, Diamandis EP, et al. Validation of biomarkers that complement CA19.9 in detecting early pancreatic cancer. Clin Cancer Res. 2014;20:5787–95.
24. Hata S, Sakamoto Y, Yamamoto Y, Nara S, Esaki M, Shimada K, et al. Prognostic impact of postoperative serum CA 19–9 levels in patients with resectable pancreatic cancer. Ann Surg Oncol. 2012;19:636–41.
25. Li B, Yin X, Ding X, Zhang G, Jiang H, Chen C, et al. Combined utility of Ki-67 index and tumor grade to stratify patients with pancreatic ductal adenocarcinoma who underwent upfront surgery. BMC Surg. 2023;23:370.
26. Pergolini I, Crippa S, Pagnanelli M, Belfiori G, Pucci A, Partelli S, et al. Prognostic impact of Ki-67 proliferative index in resectable pancreatic ductal adenocarcinoma. BJS Open. 2019;3:646–55.
27. Hu H-Y, Liu H, Zhang J-W, Hu K, Lin Y. Clinical significance of Smac and Ki-67 expression in pancreatic cancer. Hepatogastroenterology. 2012;59:2640–43.
28. Gao J, Han F, Jin Y, Wang X, Zhang J. A radiomics nomogram for the preoperative prediction of lymph node metastasis in pancreatic ductal adenocarcinoma. Front Oncol. 2020;10:1654.
29. Agostini A, Borgheresi A, Mari A, Floridi C, Bruno F, Carotti M, et al. Dual-energy CT: theoretical principles and clinical applications. Radiol Med. 2019;124:1281–95.
30. Gillies RJ, Kinahan PE, Hricak H. Radiomics: images are more than pictures, they are data. Radiology. 2016;278:563–77.
31. O'Connor JPB, Rose CJ, Waterton JC, Carano RAD, Parker GJM, Jackson A. Imaging intratumor heterogeneity: role in therapy response, resistance, and clinical outcome. Clin Cancer Res. 2015;21:249–57.
32. Attiyeh MA, Chakraborty J, McIntyre CA, Kappagantula R, Chou Y, Askan G, et al. CT radiomics associations with genotype and stromal content in pancreatic ductal adenocarcinoma. Abdom Radiol (NY). 2019;44:3148–57.
33. Kim BR, Kim JH, Ahn SJ, Joo I, Choi S-Y, Park SJ, et al. CT prediction of resectability and prognosis in patients with pancreatic ductal adenocarcinoma after neoadjuvant treatment using image findings and texture analysis. Eur Radiol. 2019;29:362–72.
34. Ichikawa T, Erturk SM, Sou H, Nakajima H, Tsukamoto T, Motosugi U, et al. MDCT of pancreatic adenocarcinoma: optimal imaging phases and multiplanar reformatted imaging. AJR Am J Roentgenol. 2006;187:1513–20.
35. Ergen B, Baykara M. Texture based feature extraction methods for content based medical image retrieval systems. Biomed Mater Eng. 2014;24:3055–62.
36. Zhang Y-P, Zhang X-Y, Cheng Y-T, Li B, Teng X-Z, Zhang J, et al. Artificial intelligence-driven radiomics study in cancer: the role of feature engineering and modeling. Mil Med Res. 2023;10:22.
37. Aerts HJWL, Velazquez ER, Leijenaar RTH, Parmar C, Grossmann P, Carvalho S, et al. Decoding tumour phenotype by noninvasive imaging using a quantitative radiomics approach. Nat Commun. 2014;5:4006.
38. Lambin P, Leijenaar RTH, Deist TM, Peerlings J, de Jong EEC, van Timmeren J, et al. Radiomics: the bridge between medical imaging and personalized medicine. Nat Rev Clin Oncol. 2017;14:749–62.
39. Haarburger C, Müller-Franzes G, Weninger L, Kuhl C, Truhn D, Merhof D. Radiomics feature reproducibility under inter-rater variability in segmentations of CT images. Sci Rep. 2020;10:12688.
40. Traverso A, Wee L, Dekker A, Gillies R. Repeatability and reproducibility of radiomic features: a systematic review. Int J Radiat Oncol Biol Phys. 2018;102:1143–58.

Publisher's Note